In situ particle size estimation for crystallization processes by multivariate image analysis

Debasis Sarkar[a], Xuan-Tien Doan[a], Zhou Ying[a], Rajagopalan Srinivasan[a,b,*]

[a]*Process Science and Modeling, Institute of Chemical & Engineering Sciences, 1 Pesek Road, Jurong Island, Singapore 627833, Singapore*
[b]*Department of Chemical and Biomolecular Engineering, National University of Singapore, 10 Kent Ridge Crescent, Singapore 117576, Singapore*

ABSTRACT

Crystal size estimation from in situ images has received attention recently as a means to estimate product properties in real-time. In this paper, an automated image analysis strategy that combines classical image analysis techniques with multivariate statistics has been developed for online analysis of in situ images from crystallization process. The strategy introduces a novel image segmentation step based on information extracted from multivariate statistical models. Experimental results for batch cooling crystallization of monosodium glutamate show that the strategy effectively extracts crystal size and shape information from in situ images. The robustness and efficiency of the method has been established by comparing its performance with those obtained by manual analysis of the images. The method yields reasonably good estimates of particle length and is also fast enough to provide online measurements for the purpose of online optimization and control of a typical crystallization process.

1. Introduction

Crystallization from solution is a widely practiced unit operation in specialty chemical, pharmaceutical, and agrochemical industries for solid-liquid separation, purification, and production of solid crystals with desired shape and size distribution. The ability to effectively control the crystal shape and crystal size distribution (CSD) is essential as it strongly influences the effectiveness of the end-use properties of the crystal products (bioavailability, compressibility, stability, dissolution rate, etc.) as well as the efficiency of downstream operations (filtration, drying, storage, handling, etc.). Since CSD is the key controlled variable, an accurate measurement of the CSD is extremely important for crystallization process control. Crystallization processes in pharmaceutical and fine chemicals manufacturing are seldom operated under advanced automatic control schemes due to lack of understanding of the process, non-availability of detailed mathematical models, and the lack of in situ sensors to directly measure the product quality (Yu et al., 2007). Currently, these processes are operated so as to follow pre-specified trajectories that are supposed to yield desired product quality, without direct online control of quality. This leads to batch-to-batch variability, unacceptably low product qualities, and overall production inefficiencies. However, the obstacles that have hindered the implementation of advanced closed-loop control in industry are being overcome by recent advances in measurement and computing technology. Although there are many techniques available to derive CSD, very few offer the opportunity for direct in-line measurement without the need for sampling or external recirculation. Thus, there is a strong motivation to have efficient in-line measurement and analysis techniques of the CSD for modeling, optimization, monitoring, and effective closed-loop control of particulate processes.

Recent years have witnessed the development and application of a variety of new online particle characterization techniques among which the ultrasonic attenuation spectroscopy (UAS) and the focused-beam reflectance measurement (FBRM) from Lasentec have emerged as the most widely used tools. The particle size distribution (PSD) and concentration of a suspension can be determined by measuring its ultrasonic velocity and/or attenuation coefficient as a function of frequency and then using a suitable mathematical model to interpret the spectra. The key advantages of UAS are its large measurement range and the ability to examine highly concentrated or optically opaque systems without the need for analyte dilution (Mougin et al., 2003). The main disadvantage of the technique, however, is that it requires a large set of accurate data related to the physical properties of both the liquid and particle phases, some of which are difficult to obtain.

* Corresponding author at: Department of Chemical and Biomolecular Engineering, National University of Singapore, 10 Kent Ridge Crescent, Singapore 117576, Singapore. Tel.: +65 65168041; fax: +65 67791936.
E-mail address: chergs@nus.edu.sg (R. Srinivasan).

The FBRM has also recently gained considerable attention for on-line particle characterization. It uses a highly focused rotating laser beam that scans across particles passing in front of the probe window to measure the chord length distribution (CLD), which is statistically related to the PSD and depends on the geometry of the crystals. The advantages of the technique include ease of use, little maintenance or calibration requirement, and capability for in situ measurement in systems with high solid concentration. In many industrial cases, CLD measurements are adequate for reliable tracking of qualitative trends in particle population. However, it is not always straightforward to obtain quantitative information by converting a measured CLD into its corresponding PSD accurately as it involves the solution of an ill-posed inversion problem. Additionally, CLD also depends on particle optical properties and focal point position. Although methods have been developed for inverting the measured CLD to obtain the PSD (Ruf et al., 2000; Worlitschek et al., 2005; Li and Wilkinson, 2005), successful application of these methods has been demonstrated experimentally only for spheres and octahedra (Larsen et al., 2007).

Image-based methods offer the potential to extract both qualitative and quantitative information of PSD based on direct visualization of the process. The rapid progress in high-speed online digital imaging sensors, such as Particle Vision and Measurement (PVM) from Mettler Toledo, Particle Image Analyzer (PIA) from MessTechnik Schwartz, In situ Particle Viewer (ISPV) from Perdix, and online microscopy from GlaxoSmithKline (Barrett and Glennon, 2002; Qu et al., 2006; Wang et al., 2008) has made image analysis a promising option for real-time measurement of particle shape and size distribution. While precise techniques for analyzing images of particles taken off-line for size and shape studies have been available and widely used (Puel et al., 1997; Sakamoto and Rousseau, 2000; Patience et al., 2004), it is only recently that the inline measurements are becoming possible and receiving increasing attention. It is not trivial to apply commercially available software developed for static image analysis directly to real-time images obtained from a process environment where images contain blurred, out-of-focus, and overlapping particles (Braatz, 2002; Wang et al., 2008). In order to be effective for online process control, image analysis needs to be accurate, fast, robust and tolerant to the quality of online images. Most publications in the area of image analysis for PSD have used the same broad steps to achieve this. The first important step is to distinguish the particles from the background, i.e., segmentation. Next, an edge detection routine is generally used to trace the approximate boundary of the particle by identifying abrupt changes in pixel intensities. Subsequently, morphological operations are performed to rectify the boundary and extract the object of interest from the image. In particular, the contours determined by edge detection are filled, regions that touch image border eliminated, and each unconnected region that represents an object filled to locate the object. Finally, geometrical properties of the identified object, such as maximum chord length or best-fit minimum-area rectangle, are measured to extract particle features.

Robust segmentation remains the main barrier to successful automation of image analysis (Larsen et al., 2006). Calderon De Anda et al. (2005a) developed a multi-step multi-scale segmentation methodology for quantitative analysis of images of different crystal morphological forms and of varied qualities obtained using the GlaxoSmithKline imaging system. Their image analysis technique involves multi-scale edge detection using the Canny method followed by object segmentation. Application of the methodology has been shown to be effective for real-time monitoring of crystal polymorphic and morphological forms (Calderon De Anda et al., 2005b), and also for the estimation of the growth rates of individual crystal facets (Wang et al., 2007; Ma et al., 2007). Attempts have also been made to obtain 3-D shape information from 2-D online images (Li et al., 2006). Recently, Wang et al. (2008) extended the multi-scale segmentation methodology for analysis of online video images of crystallization at high-solid concentrations where crystals tend to overlap and boundaries between the crystals are ambiguous. Qu et al. (2006) developed a similar image analysis method based on two-stage edge detection to study the effects of additives in a batch cooling crystallization process. Larsen et al. (2006) developed a model-based image analysis algorithm for in situ images of suspended, high-aspect-ratio crystals for moderate solids concentrations. The algorithm is based on the assumption that a needle-shaped crystal can be modeled geometrically as a group of two or more spatially proximate lines with similar orientation and length. Larsen et al. (2007) further extended the model-based object recognition algorithm for crystals of any shape, provided the shape can be represented as a wire-frame model. The algorithms are reported to be sufficiently fast and accurate to enable real-time monitoring and control. Recently, Dahl et al. (2007) developed an image analytical technique for the determination of PSD characteristics of natural and industrial bulk aggregates based on Angle Measure Technique (AMT), multivariate data analysis (partial least square regression), and theory of sampling. The applicability of the methodology has been demonstrated by determining the size distributions of sand mixtures of varying composition. More recently, Kempkes et al. (2007) proposed a model for rapid processing of CLD data (from FBRM) as well as in situ microscopy data (from PVM) to monitor the evolution of size and shape of crystals in a suspension during growth and to extract information about their growth kinetics. The model assumes convex polyhedral particles that are defined by their vertices only, connected by straight lines, but imposes no further restrictions on the particle geometry.

Although high-speed, in situ imaging and image analysis techniques have been shown to be a promising technology for particulate processes, automatic extraction of the desired information from in situ images in a robust and efficient manner still remains challenging (Larsen et al., 2007). The goal of the present study is to develop a fully automated and efficient methodology for real-time analysis of in situ images from crystallization processes. Specifically, we combine multivariate image analysis with classical image analysis technique for online extraction of both qualitative and quantitative information about the PSD, which can in the future be used for process monitoring and closed-loop control. The in-line imaging instrument employed in this study is a PVM. However, the strategy developed for image analysis is general and not limited to images from PVM alone. Segmentation is performed using a multivariate statistical model of the blank background (without particles). Particles are isolated in other in situ images by comparison with the background model. This is in contrast to the existing image analysis strategies where models of particles are usually considered. Batch cooling crystallization of monosodium glutamate (MSG) is chosen as a reference system. The robustness and accuracy of the measured PSD by the algorithm for this system is demonstrated with respect to the measurements obtained through manual segmentation by human operators. Our results show that the accuracy of the measured PSD compares favorably with respect to the manual segmentation and seems suitable for real-time monitoring and control of such crystallization processes. Although the application of the developed strategy is focused on MSG crystallization process, the methodology may be extended to other particulate processes as well.

The rest of the paper is organized as follows. In Section 2, we give a brief overview of multivariate image analysis. Next, we present the development of the proposed image analysis strategy in detail in Section 3. Section 4 presents the experimental study and the validation of the approach. Finally, conclusions are drawn in Section 5.

2. Multivariate image analysis: a brief overview

The goal of multivariate image analysis (MIA) methods is to extract significant information from an image while reducing the dimensionality of the image data. MIA techniques, originally introduced by Esbensen and Geladi (1989), have been extended and widely used for chemical process monitoring and control by MacGregor and coworkers (See Bharti and MacGregor, 1998; Yu et al., 2003; Bharti et al., 2003; Bharati et al., 2004; and references therein). Essentially, MIA involves performing multiway principal component analysis (MPCA) on a multivariate image that divides information into orthogonal components by transforming the image into a number of principal components (latent or score images). A multivariate image consists of a stack of congruent images of the same scene or object, with each image in the stack representing a unique variable, such as a primary color. Such an image can be represented as a three-dimensional data set, where two dimensions (x and y) represent the image plane and the third dimension (z) represents the variable (color) index. MPCA of such a three-dimensional ($n_x \times n_y \times n_z$) image array $\underline{\mathbf{X}}$ decomposes it into N_p ($< n_z$) principal components (PCs) consisting of ($n_x \times n_y$) score matrices $\mathbf{T}_a$ and ($n_z \times 1$) loading vectors $\mathbf{p}_a$ plus a residual array $\underline{\mathbf{E}}$, i.e.

$$\underline{\mathbf{X}} = \sum_{a=1}^{N_p} \mathbf{T}_a \otimes \mathbf{p}_a + \underline{\mathbf{E}} \tag{1}$$

where $\otimes$ denotes the Kronecker product (Bharti and MacGregor, 1998). The principal components are extracted in order of decreasing variance such that the first component explains the greatest amount of variance in $\underline{\mathbf{X}}$, the second component the next greatest variance, and so forth. The score matrices have the same size as the original images and can be interpreted as latent variable images in the original image space. The loadings $\mathbf{p}_a$ express the contributions of the score images to the raw images. It is usually found that much of the information in the original image data is expressed in terms of only the first few PCs.

The above method of MPCA is equivalent to unfolding the three-dimensional matrix $\underline{\mathbf{X}}$ into an extended two-dimensional matrix $\mathbf{X}$ and then performing ordinary PCA on it

$$\underset{n_x \times n_y \times n_z}{\mathbf{X}} \xrightarrow{\text{unfold}} \underset{(n_x \cdot n_y) \times n_z}{\mathbf{X}} = \sum_{a=1}^{N_p} \mathbf{t}_a \mathbf{p}_a^T + \mathbf{E} \tag{2}$$

where $\mathbf{t}_a$ is an ($n_x \cdot n_y$) $\times 1$ score vector and $\mathbf{p}_a$ is an ($n_z \times 1$) loading vector. The score vectors $\mathbf{t}_a (a = 1, \ldots, N_p)$ are constrained to be orthogonal, and the loading vectors $\mathbf{p}_a$ ($a = 1, \ldots, N_p$) are orthonormal.

MIA methods have been successfully used for monitoring and control of various processes, such as snack food processes (Yu et al., 2003) and floatation froth processes (Liu et al., 2005; Bartolacci et al., 2006). The information content in the image is usually extracted from the individual pixels through a scatter score plot of the dominant principal components. Unlike in situ images from a crystallizer that suffer from numerous aberrations such as background noise, bubbles, out-of-focus objects, and particles in motion, the images in these applications have fewer imperfections. In order to extract particles from in situ images, the MIA approach therefore, has to be extended and combined with image analysis approaches as described next.

3. Multivariate image analysis strategy for particle characterization

The proposed image analysis strategy is based on the principle that the desired objects (particles) can be segmented from the image frames by eliminating those parts that represent the background.

The algorithm comprises two stages: a one-off learning stage where a model of the background is built and a real-time image processing stage where particles are segmented from in situ images. In the learning stage, a training image of the background at the start of crystallization is taken and its multivariate feature image generated. Subsequently, a *pseudo-image* of the background is developed as explained in detail later and its statistical characteristics extracted. In the real-time image processing stage, the same procedure is followed for each image captured inline by the PVM probe. The two pseudo-images are then compared statistically to isolate regions that are *not* background, i.e., particles. Critical solid-phase properties such as particle size and shape distribution can then be determined by a series of classical image analysis steps during the post-segmentation operations. In what follows, we describe these steps in detail.

3.1. Extraction of image features

The key observation in MIA is that the score matrices are themselves images (Geladi et al., 1989) and hence can be analyzed using common classical image analysis techniques. However, it may be noted that when the three-dimensional multivariate image matrix is unfolded into a corresponding two-dimensional matrix, the MPCA method treats each pixel as a separate object independent of its neighbors. This breaks the spatial relationships in the image. Since MIA does not explicitly account for local spatial variations in the image, it can not enable segmentation. For example, if two pixels have the same intensities, they will have the same scores in the score image obtained from MIA, regardless of the intensities of other pixels in their respective neighborhoods. Spatial relationships are critical to locating objects in an image. For instance, when the pixel intensities change rapidly in a small neighborhood, it indicates an object boundary. The loss of spatial information may be regained by (1) properly using features that capture neighborhood (spatial) information, as well as (2) augmenting each pixel with information about its neighbors. We use both these schemes in this work.

The first step towards feature extraction is to choose a feature that characterizes the object of interest in the image thus leading to its efficient segmentation. It is intuitive that more than one feature would facilitate the process. In this study, various texture and edge features, such as range, standard deviation, entropy, edge emphaszier, and variogram have been evaluated for their efficiency in particle characterization.

Each image ($f(x, y)$), captured by the PVM probe, is a matrix of pixels (say 640×480), and the value (f) at each location (x, y) is in the gray-scale intensity range of 0–255: 0 denoting black and 255 white. At each pixel, a neighborhood can be defined. We have used a square window of size B centered on the pixel as the neighborhood, although other shapes such as circle or ellipse can also be used.

Range is the difference between the maximum and minimum intensities of the input pixels. The range value at each pixel in a PVM image is evaluated using the gray-scale intensities of the corresponding pixel as well as the pixels in the neighborhood as follows:

$$f_{\text{range}}(x, y) = \max_{\substack{i \in (x-B, x+B) \\ j \in (y-B, y+B)}} \{f(i,j)\} - \min_{\substack{i \in (x-B, x+B) \\ j \in (y-B, y+B)}} \{f(i,j)\} \tag{3}$$

The range feature detects edges in the neighborhood and thereby helps in image segmentation.

Standard deviation measures the variation in the intensities of the input pixels. This feature value is evaluated using the intensities of the pixels in the neighborhood as follows:

$$f_{\text{std}}(x, y) = \sigma_{\substack{i \in (x-B, x+B) \\ j \in (y-B, y+B)}} \{f(i,j)\} \tag{4}$$

where σ represents the standard deviation. The pixels within a particle have higher standard deviation values which helps in separating particles from the background.

The *edge feature* seeks to highlight the boundary of an object (such as a particle) in a gray-scale image. This is typically indicated by a change in the intensity over a small neighborhood. Therefore, the derivative of the intensity as a function of the position can be used to detect the presence of an edge. Similar to the Sobel edge detection filter for extracting edge features (Gonzalez et al., 2004), the horizontal and vertical gradients at each pixel are extracted using a horizontal (A_X) and vertical (A_Y) kernel as follows:

$$A_X = \begin{vmatrix} 1 & 2 & 1 \\ 0 & 0 & 0 \\ -1 & -2 & -1 \end{vmatrix}$$

$$A_Y = \begin{vmatrix} 1 & 0 & -1 \\ 2 & 0 & -2 \\ 1 & 0 & -1 \end{vmatrix}$$

$$G_X(x,y) = \sum_{i=1}^{3}\sum_{j=1}^{3} f(x+i-2, y+j-2)A_X(i,j) \tag{5}$$

$$G_Y(x,y) = \sum_{i=1}^{3}\sum_{j=1}^{3} f(x+i-2, y+j-2)A_Y(i,j) \tag{6}$$

These respond maximally to edges vertically and horizontally and can be combined together to find the absolute magnitude of the gradient (f_{edge}) at each point as follows:

$$f_{\text{edge}}(x,y) = \sqrt{G_X^2(x,y) + G_Y^2(x,y)} \tag{7}$$

Entropy is a statistical measure of randomness that can be used to characterize the texture of the input image. Entropy is defined as

$$f_{\text{entropy}}(x,y) = - \sum_{\substack{i \in (x-B, x+B) \\ j \in (y-B, y+B)}} p(f(i,j))\log_2 p(f(i,j)) \tag{8}$$

where $p(f(i,j))$ is the histogram of the intensity levels in the neighborhood.

The *variogram* feature makes it possible to take into account the spatial distribution of the pixels in a neighborhood. It describes the degree of spatial dependence of the pixels in a neighborhood and can be computed between two pixels v_i and $v_i + \mathbf{h}$ as follows:

$$f_{\text{variogram}}(x,y) = \frac{1}{2n(\mathbf{h})} \sum_{k=1}^{n(\mathbf{h})} [f(v_k) - f(v_k + \mathbf{h})]^2 \tag{9}$$

where $\mathbf{h}$ is a vector with a specified direction and length, $n(\mathbf{h})$ is the number of pairs of pixels (in the neighborhood) that are $|\mathbf{h}|$ pixels apart in $\mathbf{h}$ direction.

Each of the above features results in a matrix that has the same size as the original image and can be viewed as an image itself. We can now stack the individual feature images on top of each other to form a multi-way feature matrix $\underline{\mathbf{X}}_f$ as follows:

$$\underline{\mathbf{X}}_f = [f_{\text{range}}; f_{\text{std}}; f_{\text{edge}}; \ldots] \tag{10}$$

In order to further emphasize spatial information, we augment each pixel in the image with its neighbors. This is achieved by shifting the feature image by r_s pixels (shifting radius) within the image plane in eight different directions as shown in Fig. 1 (Bharati et al., 2004). The shifted images are then stacked and cropped at the edges to eliminate the non-overlapping segments thus resulting in eight congruent images for each feature. This is repeated for each feature. The resulting three-dimensional matrix ($\underline{\mathbf{X}}$) is unfolded into
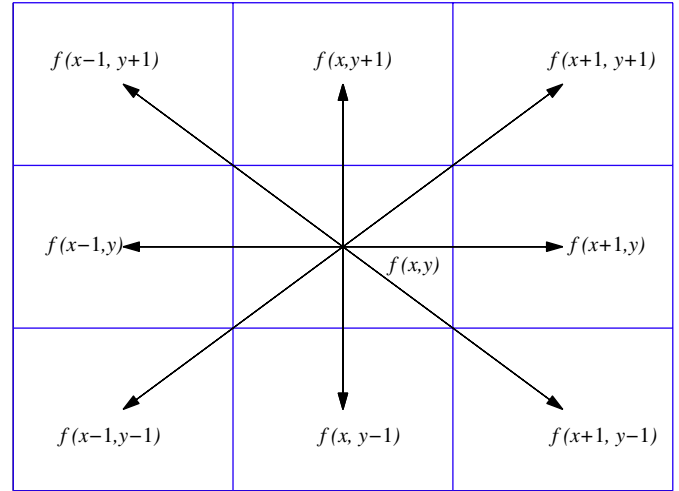

Fig. 1. Scheme for creating a multi-way image from each feature image by spatial shifting in eight adjacent directions.

an extended two-dimensional matrix and PCA performed to extract scores and loadings.

3.2. Statistical image model and segmentation

Each of the score matrices can be interpreted as a 2-D image and can be used to represent the original image. We term this as a pseudo-image. While the first PC explains the greatest amount of variance in the image data, it is noticed that with increase in the number of features, the fraction of variance explained by the first PC decreases. It is necessary to consider several ($N_p > 1$) PCs to build a representative pseudo-image so that the cumulative variance captured by the PCA model is significant (say $\geqslant 93\%$). Hotelling's T^2 statistics emerges as the natural choice to incorporate several PCs into a single pseudo-image as follows:

$$T_{N_p}^2 = \sum_{i=1}^{N_p} \frac{\mathbf{t}_i^2}{\mathbf{s}_{t_i}^2} \tag{11}$$

where $\mathbf{s}_{t_i}^2$ is the estimated variance of the score vector $\mathbf{t}_i$ and N_p is the number of PCs retained. Although the T^2 image has the same size as the original image, the square function systematically introduces a nonlinearity which emphasizes different pixel ranges differently—high pixel-values are over-emphasized while low-pixel values are under-emphasized. Since information in images are distributed at both the high and low ranges, this non-linearity is undesirable. We therefore use a square-root transformations of the T^2 image in order to regain homogeneity. The fact that square root operation is an effective filter for the T^2 model image can be easily seen from Fig. 2 where we plot, for a sample image, both the T^2 and $\sqrt{T^2}$ images. It is obvious from Fig. 2 that the square root filtered image provides a much better representation of the original image than the T^2 image on the basis of visual evaluation. Therefore, we consider $\sqrt{T^2}$ statistic as the model for the original image. Subsequently, segmentation is performed on this pseudo-image $X^p = \sqrt{T^2}$ to extract particles. The objective of image segmentation is to find those sets of pixels that correspond to distinct particles. While the original in situ images are often blurred and have non-uniform background pixel intensity, the pseudo-image (X^p) has fewer imperfections. Therefore particle boundaries can be reliably identified by thresholding the gray-level pseudo-image to a binary image $g(x,y)$ that retains all the

Fig. 2. (a) An in situ image and its pseudo-images using (b) Hotelling's T^2 statistics, and (c) $\sqrt{T^2}$ statistics.

relevant information concerning the number, position, and structure of the particles that are present in the gray-level image.

$$g(x,y) = \begin{cases} 1 & \text{if } X^p(x,y) \geqslant \psi_s \\ 0 & \text{else} \end{cases} \tag{12}$$

where ψ_s is a global threshold. Thresholding classifies the image pixels according to their values into two classes, the particle class (1) and a background class (0).

A key issue in any thresholding scheme is to select the value of the threshold. In our work, we parameterise ψ_s on the pseudo-image X^p_{BG} corresponding to the blank background image of the crystallization solution.

$$\psi_s = \alpha \sigma(X^p_{BG}) \tag{13}$$

where σ is the standard deviation of the pixels in X^p_{BG} and α is a user-defined parameter that is a measure of the level of confidence on the model of the background image. Our choice of ψ_s is thus based on global information of the background image. Segmentation is effected by comparing the regions of similarity according to ψ_s between statistical models of the background and in situ images.

After thresholding, the image is segmented into many regions which are sets of connected pixels of the same class (particle or background). However, the class assignment at this stage is not perfect and more often than not, parts of a particle would be missing or disjoint. Post-segmentation image analysis seeks to rectify the classification using classical image analysis approaches.

3.2.1. Post-segmentation image analysis

Since the binary image obtained after thresholding may contain many artifacts in the form of tiny isolated structures and small holes within particles, a flood-fill operation is first performed on background pixels of the binary image to fill holes. This image is then opened morphologically to remove all small objects below a specified pixel area threshold ψ_a, followed by labeling of all the connected components. Objects on the boundary of the image are removed. The remaining objects are shortlisted as particles and their exterior boundary identified.

3.3. Boundary refinement

The boundary of a segmented region is the set of pixels in the region that have one or more neighbors that do not belong to the region. There are several ways to represent a boundary: Freeman chain coding, polygonal approximation, skeletons, etc. In this work, we select Fourier descriptors to describe the boundary of the segmented objects. In a two-dimensional xy-plane, an object boundary $\bar{\mathcal{O}}$ can be represented as a sequence of coordinates of its K pixels, arranged in clockwise or counter-clockwise direction.

$$\bar{\mathcal{O}} = [\bar{v}_1, \bar{v}_2, \ldots, \bar{v}_k, \ldots, \bar{v}_K] \tag{14}$$

where $\bar{v}_k = [\bar{v}_k^x \ \bar{v}_k^y]^T$ indicates the x and y coordinates of the kth boundary pixel. Treating each $\bar{v}_k$ as a complex number, $\bar{v}(k) = \bar{v}_k^x + j\bar{v}_k^y$, a discrete Fourier transform can be obtained as

$$a(u) = \sum_{k=0}^{K-1} \bar{v}(k) e^{-j2\pi uk/K} \quad \forall u = 0, 1, \ldots, K-1 \tag{15}$$

where the complex coefficients $a(u)$ are the Fourier descriptors of boundary $\bar{\mathcal{O}}$. The coefficients $a(u)$ at lower u represent lower frequency components, and describe the macro shape of $\bar{\mathcal{O}}$. On the other hand, those at higher u correspond to higher frequency components and account for fine details of the boundary. To eliminate noise, we reconstruct the macro shape $\mathcal{O}$ using $N_{FC} < K$ components of the coefficients $a(u)$, through inverse Fourier transform.

$$v(k) = \frac{1}{N_{FC}} \sum_{u=0}^{N_{FC}-1} a(u) e^{-j2\pi uk/N_{FC}} \quad \forall u = 0, 1, \ldots, N_{FC}-1 \tag{16}$$

$$\mathcal{O} = [v_1, v_2, \ldots, v_k, \ldots, v_K] \tag{17}$$

A shape-based *signature curve*, which is a 1-D functional representation of 2-D smoothed boundary, is then used to evaluate the effectiveness of the resulting segmentation. The signature curve is generated by plotting the distance r from the center of the segmented object to the pixels on the boundary as a function of angle, ϕ. The function $r(\phi)$ is periodic, with a period of 360°. If the 2-D particle shape is known a priori (e.g. ellipse, rectangle), a mathematical formulation of $r(\phi)$ can be obtained by fitting the observed boundary points to the expected signature curve. At the minimum, vertices of the segmented object can be identified directly, since vertices would correspond to maxima in the signature curve. The sequence of the maxima characterize the size and shape of the segmented object. For example, if a particle has a rectangular shape on the 2-D image, its signature curve would have four maxima. Also, the maximal chord length (MCL) of the particle would correspond to the largest Euclidean distance between the vertices. Ideally, the MCL would be the distance between two vertices that are 180° apart. If the segmentation of the particles is not perfect, the resulting signature curve may be noisy, and the peaks may shift and therefore not exactly 180° apart. Hence, we introduce a threshold (θ_a) called the antipodal angle threshold. To calculate the MCL, we consider the maximum distance between any two vertices that are 180° ± θ_a apart. Instances when two peaks are apart by over 180° ± θ_a are discarded as incorrectly segmented. Thus the characteristics of the signature curve forms the basis for evaluating the particle size as well as the effectiveness of particle segmentation. Fig. 3 illustrates the above boundary refinement steps.

4. Case study: Batch crystallization of MSG

The performance of the proposed image analysis methodology is evaluated in a case study on seeded batch cooling crystallization
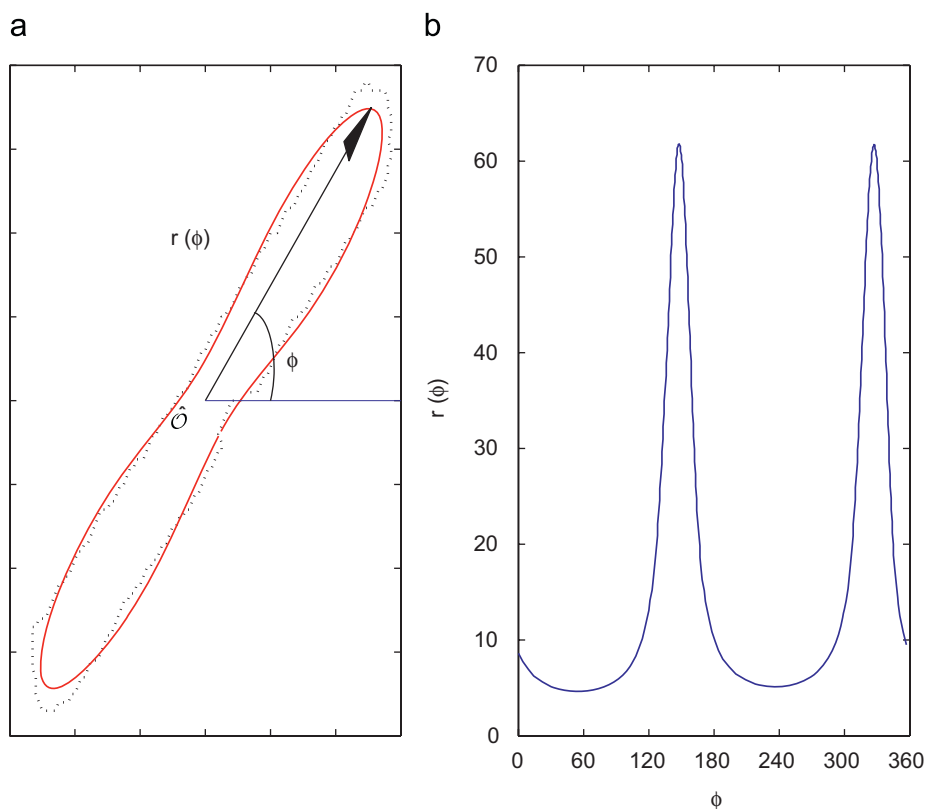
a

b

Fig. 3. (a) Refined boundary (solid line) of the segmented region by Fourier transformation of the outline (dotted line). (b) signature curve.

Overhead stirrer

Particle Vision and Measurement (PVM) Probe

Thermocouple for Crystallizer
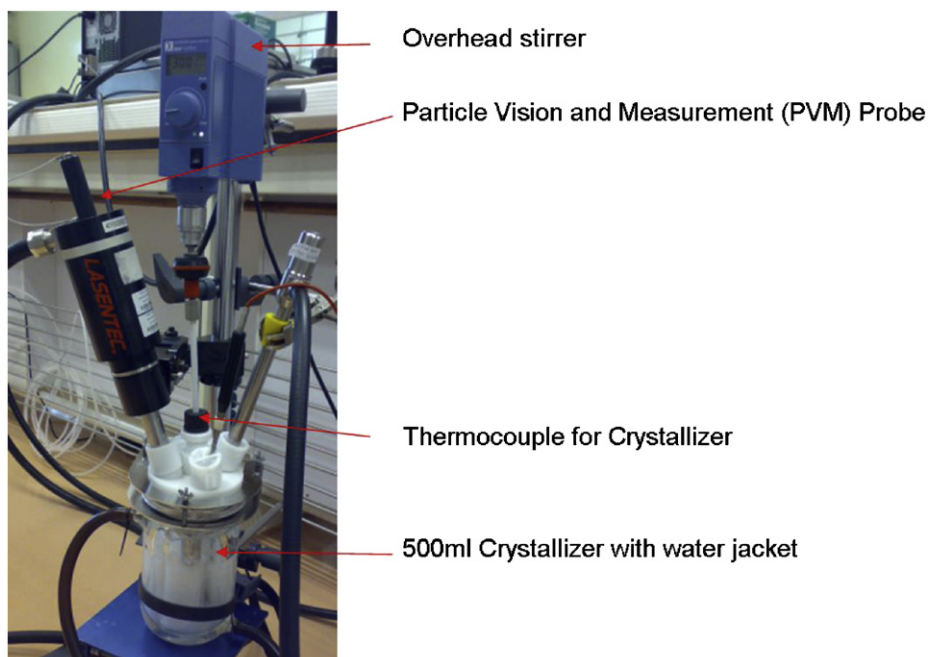
500ml Crystallizer with water jacket

Fig. 4. Experimental set-up.

of monosodium glutamate monohydrate (MSG, $C_5H_8NO_4Na \cdot H_2O$; molecular weight, 187.14). The experimental setup for the crystallization study is shown in Fig. 4. A 500 ml flat-bottomed glass vessel, fitted with an impeller driven by a variable speed overhead stirrer motor, is used as the crystallizer. An aqueous solution is prepared by

dissolving 320 g of MSG (> 98% purity from Sigma-Aldrich) in 400 ml deionized water. The solution is then heated to 80 °C in 30 min and maintained at 80 °C for another 30 min to ensure complete dissolution of all MSG particles. The solution is then cooled to 50 °C in 30 min by applying a constant cooling rate of 1 °C/min. The solution

is further cooled to 30 °C in 40 min with a constant cooling rate of 0.5 °C/min and kept constant at this temperature till the end of experiment (23 h). Seeds are prepared by grinding MSG to a sieve size of 38–45 μm. One gram of the seed is added to the solution when it reaches 40 °C during cooling. The agitation speed is kept at 350 rpm throughout the crystallization and the temperature of the crystallizer controlled by a Julabo circulator. A PVM probe (Mettler Toledo, model V700) is inserted at an angle of 45° into the suspension. In situ images are captured for the entire duration of experiment at a speed of two images per second.

The proposed image analysis strategy is implemented in Matlab® and all the computations are performed on a personal computer with 2.99 GHz CPU and 1 GB RAM running Windows XP. We use the Matlab® Image Processing Toolbox for all the classical image processing steps such as morphological opening and labeling. All the operations with the toolbox have been performed with default parameter setting. The proposed method described in Section 3 was applied using the user-defined parameters listed in Table 1. Fig. 5 illustrates the performance of our image analysis strategy for some sample images during various stages of the crystallization process. The figures clearly demonstrate the ability of the methodology to automatically segment crystals of various sizes and shapes. The three images (a,c,e) correspond to the states of the process at 85, 305, and 1035 min, respectively and represent early, intermediate, and advanced stages of the crystallization. It is obvious from the figures that the MSG crystals grow predominantly in the direction of length yielding rod like crystals. The figures also highlight that the degree of

particle overlap increases significantly as the process proceeds due to increase in solids concentration.

Fig. 6 shows the evolution of the median crystal length (D_{50}) with time. The lengths presented are the median obtained from all the particles detected in a time interval of 60 min. It can be seen that the crystals grow in length from about 86 to 306 μm in 23 h of operation. The other measures of population length also reveal a similar trend. For example, the mean length (D_{32}) of the crystals (data not shown) increases from about 105 to 340 μm. A similar analysis for the width of the particles (data not shown) reflects that the crystals do not grow much along their width for this system and remains almost constant at about 15 μm. Thus the growth rate is clearly different for different facets and the image analysis methodology can be used to investigate the crystal growth rates in different dimensions. Fig. 7 shows the cumulative particle size (length) distribution at different times (2, 6, 10, and 22 h) during the course of crystallization. The figure shows the percent (fraction) of particles smaller than a given size, defined as the cumulative number percent undersize. Crystal sizes corresponding to specific percentile values can be read directly from

Table 1
Parameter values.

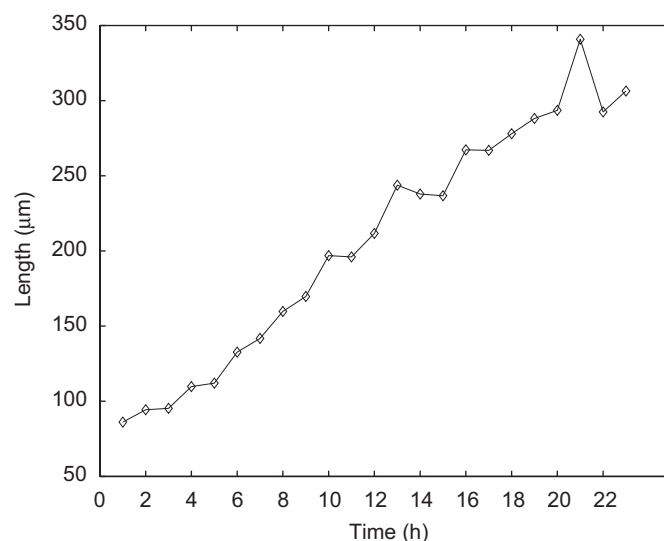| Parameter	Value
Features selected	Range
	Standard deviation
	Edge emphasizer
Number of PCs retained, N_p	6
Threshold parameter, α	2.5
Pixel area threshold, ψ_a	200
Neighborhood size, B	3
Radius of shifting, r_s	1
Number of Fourier coefficients for boundary refinement, N_{FC}	10
Threshold on antipodal angle, θ_a	35°

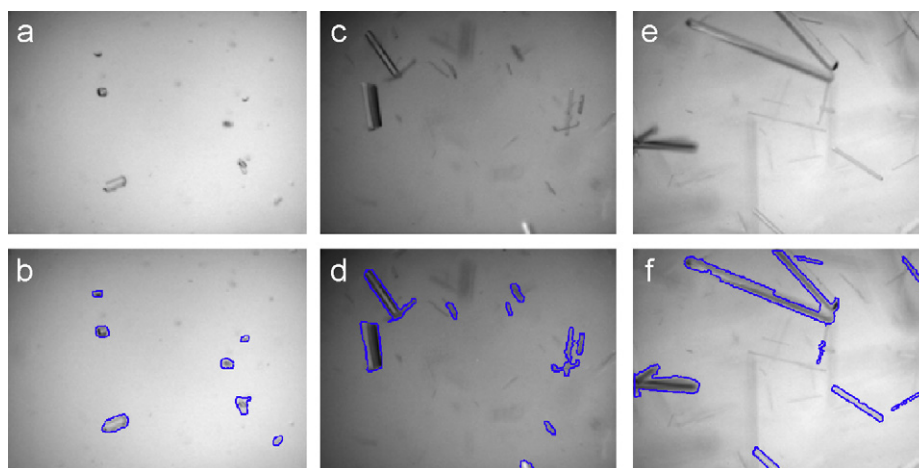**Fig. 6.** Time evolution of hourly average of median particle length during crystallization.

Fig. 5. Results of applying the proposed image analysis strategy on PVM images from MSG crystallization process. (a),(c),(e): in situ images at 85, 305, and 1035 min, respectively. (b),(d),(f): particles identified after automatic segmentation.
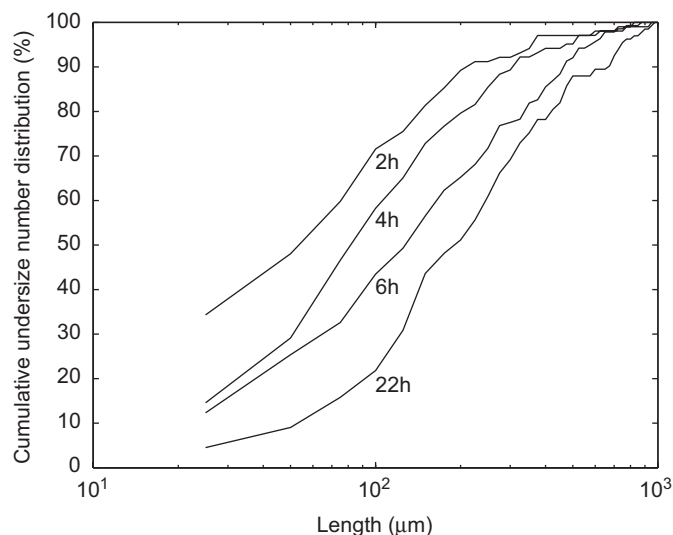
Fig. 7. Evolution of cumulative particle size distribution during crystallization.

Table 2
Difference in results between manual and automated particle sizing.

Tolerance factor (δ)	Particles matched (%)	Median error (%)
0.1	76.64	4.26
0.2	87.18	5.06
0.3	91.89	5.45
0.4	93.74	5.66
0.5	95.19	5.84
0.6	96.14	5.92
0.7	96.88	5.96

The position of a particle in an image as determined by its outline can be characterized by its centroid.

$$\hat{\mathcal{O}} = \frac{1}{K}\sum_k v_k = \left[\frac{1}{K}\sum_k v_k^x \frac{1}{K}\sum_k v_k^y\right]^{\mathrm{T}} \tag{20}$$

The length $\|\mathcal{O}\|$ and position $\hat{\mathcal{O}}$ of the particle as derived from its outline completely characterize the particle. Other attributes such as the angle of the major axis can also be included, if necessary. This characterization enables a systematic comparison of particles identified by the two different segmentation approaches.

Two particle outlines, $\mathcal{O}_A$ and $\mathcal{O}_M$, resulting from the automatic and manual segmentations of the same image can be said to correspond *iff*:

$$\frac{d(\hat{\mathcal{O}}_A, \hat{\mathcal{O}}_M)}{\|\mathcal{O}_M\|} \leqslant \delta \tag{21}$$

where δ is an user-defined threshold. For any particle P that has corresponding outlines in the two segmentations, the error in the length estimates is given by

$$\varepsilon_P = \left|\frac{\|\mathcal{O}_A\| - \|\mathcal{O}_M\|}{\|\mathcal{O}_M\|}\right| \tag{22}$$

Statistical properties such as median error can be calculated from the errors of all corresponding particles in the two segmentations of image G.

$$E_G = \operatorname*{median}_{P \in G}(\varepsilon_P) \tag{23}$$

Similarly, a cumulative error E can be calculated for all the images in a set.

$$E = \operatorname*{median}_{\forall G}(E_G) \tag{24}$$

E thus characterizes the similarity between the automatic and manual segmentations. We choose seven tolerance factors starting from a low tolerance of $\delta = 0.1$ to a high tolerance of $\delta = 0.7$ and evaluate the percentage of particles matched for the two segmentations (manual and automatic) and the cumulative error in the size measurement for each value of δ. Table 2 presents this result in detail. It may be noted that even for a very low tolerance factor of $\delta = 0.1$, about 76% of the particles in template are detected by our approach, and the associated median cumulative error E in particle size is as low as 4.26%. More than 90% particles are detected if we increase the tolerance slightly to $\delta = 0.3$. For a high tolerance factor of $\delta = 0.7$, about 97% of particles in the template are detected, and the cumulative error increases only to about 6%. Therefore, it may be concluded that the approach maintains a good agreement with the results obtained by manual segmentation.
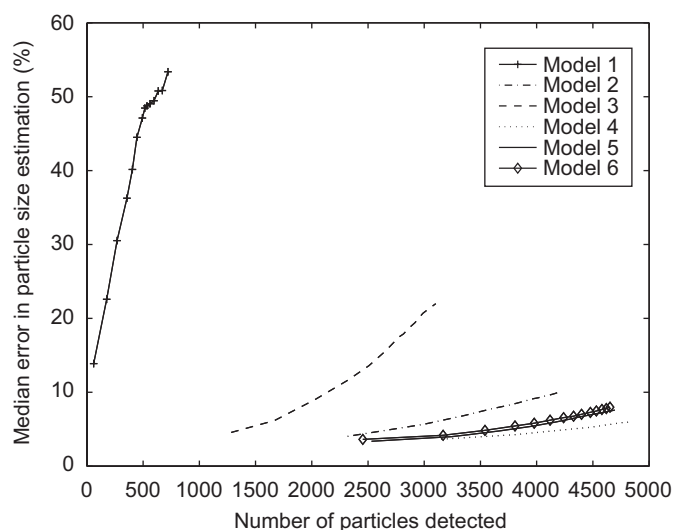
the curves plotted on semi-logarithmic scale. These cumulative size distribution curves, if adequately sampled, can provide complete information on the range of sizes present in the crystallizer. Such real-time measurements of length, width and their distribution are extremely useful not only for online optimization and control, but also for general validation of crystallization models based on multi-dimensional population balance equations.

4.1. Performance evaluation through comparison with manual segmentation

The robustness and accuracy of the obtained particle sizes was established by comparing the measurements obtained with those from manual image segmentation by human operators (Zhou et al., 2008). For this, we evenly selected 2781 images from all the images captured during the entire course of crystallization and manually segmented the crystals in the selected images by carefully drawing outlines around some of the clearly identifiable particles. These manually segmented images form a set of templates that serve as a standard for comparison. A total of 4970 particles were identified by manual size analysis; from these relevant information such as particle shape, size, and location were extracted. To evaluate the performance of our strategy for automatic particle sizing, we first determine if a particle has been detected by both approaches. We then quantify the differences in the size estimate by calculating an error metric as described next.

Consider an image G containing several particles. The image when segmented by the automatic image analysis algorithm results in a set of particles S_A that contain the outlines of the constituent particles. The manual segmentation of the same image also results in a similar set of particles S_M and their outlines. The distance between any two pixels (v_k, v_l) in the outline $\mathcal{O}$ can be calculated by the Euclidean distance between them.

$$d(v_k, v_l) = \sqrt{(v_k^x - v_l^x)^2 + (v_k^y - v_l^y)^2} \tag{18}$$

The maximum chord length of a particle, as calculated from its outline $\mathcal{O}$, can then be expressed as

$$\|\mathcal{O}\| = \max\{d(v_k, v_l)\} \quad \forall k, l \tag{19}$$

Fig. 8. Effect of features on accuracy of particle size estimation.

Fig. 9. Distribution of PCs required for capturing 93% variance.

Table 3
Selection of pseudo-image and features.

Model no.	Type of pseudo-image	Features selected	No. of PCs retained
1	Raw image	None	–
2	First score	Range, standard deviation	1
3	First score	Range, standard deviation, edge emphasizer	1
4	$\sqrt{T^2}$	Range, standard deviation, edge emphasizer	6
5	$\sqrt{T^2}$	Range, standard deviation, variogram	6
6	$\sqrt{T^2}$	Range, standard deviation, edge emphasizer, variogram	10

4.2. Effect of parameters

The proposed image analysis strategy can be considered as a hybrid scheme combining multivariate statistics and classical image processing steps. As stated earlier, the classical image processing steps have been performed with the default parameter settings of the Matlab® Image Processing Toolbox; no attempt has been made to enhance the accuracy of the image analysis by fine-tuning these parameters. The effect of the parameters in the multivariate analysis steps (Table 1) on the results has been extensively studied as summarized below.

The first step in implementing the proposed image analysis strategy is to decide how the pseudo-image has to be developed. Therefore, some of the important decision that need to be taken at the beginning are the selection of features and the number of PCs to be retained. As stated earlier, various features , such as range, standard deviation, and entropy can be used. The selection of the features in the present work has primarily been based on the accuracy of results. Fig. 8 compares the accuracy of six different models listed in Table 3. When comparing the first-score based model for three different cases: (1) raw image, i.e., without any feature extraction, (2) pseudo-image derived from range and standard deviation, and (3) pseudo-image from range, standard deviation, and edge-emphasizer features, in all cases the proposed Hotelling's T^2 pseudo-image is found to be superior. It may be noted that all models based on T^2 (Models 4, 5, and 6) are comparable to a certain extent. It may also be noted that the consideration of the first-score pseudo-image yields poorer performance as the number of features increases (compare Models 2 and 3) because the features distribute the variance in
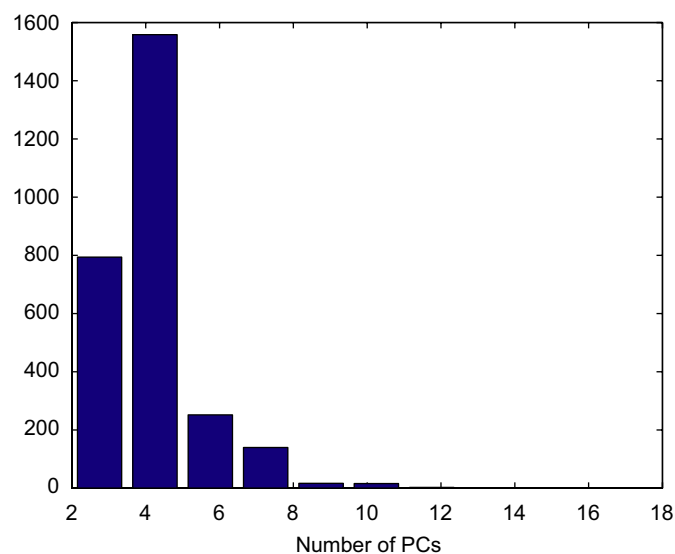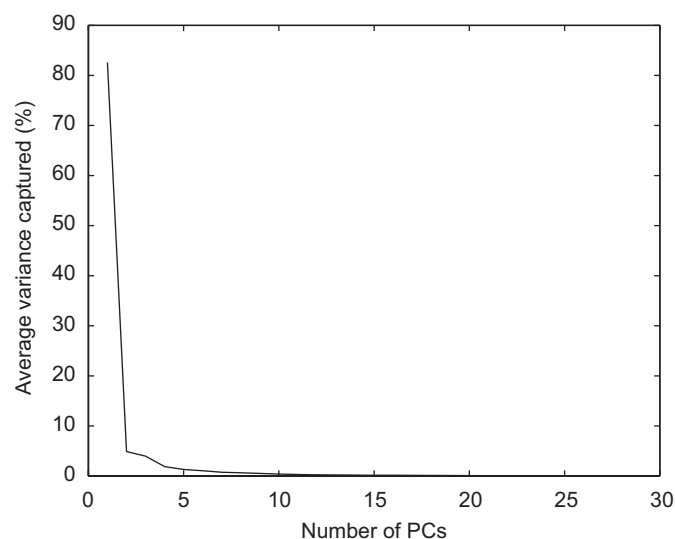

Fig. 10. Average variance captured by PCs.

the image and the first-score alone cannot provide a representative model. This clearly justifies our use of the T^2 statistic to combine information from multiple PCs.

The number of PCs to be retained in the T^2 statistics is another important consideration. We have determined this as the number of PCs that cumulatively explain a minimum of 93% of the variance in the original data. Since the in situ images captured by PVM are all of widely different qualities, the extent of variance captured by PCs is different for different images. For the three features selected, the number of PCs that can cumulatively explain a minimum of 93% variance in the image data varies from 2 to 13 (with a population average of 4.35) when tested over a large number of images. Fig. 9 presents a histogram of the distribution of PCs in capturing a minimum of 93% variance in the original image data and Fig. 10 shows the % of variance explained by the PCs. From these, we decided to retain six PCs. Fig. 11 presents the effect of number of PCs retained on the results accuracy. The cumulative error plateaus for all models with four or more PCs. Similarly, the average error does not improve beyond six PCs . It is therefore clear that additional PCs have
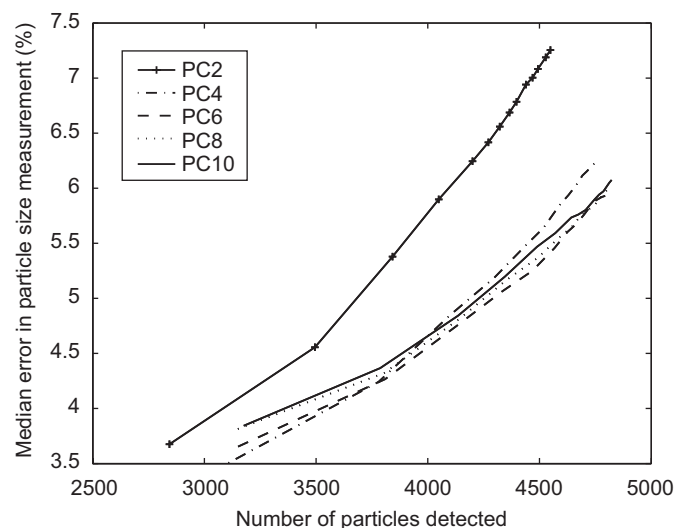
Fig. 11. Effect of number of PCs retained on the accuracy of particle size estimation.
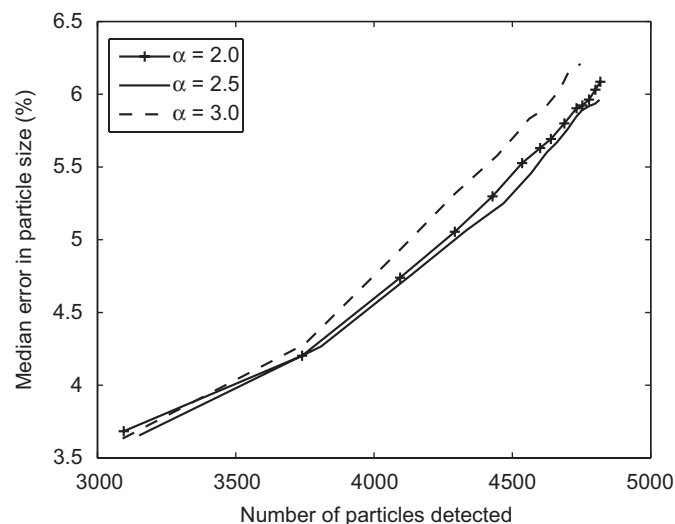

Fig. 12. Effect of α on the accuracy of particle size estimation.

practically no effect primarily because the rest of the PCs essentially capture noise.

A key feature of our image analysis strategy is the image segmentation based on the multivariate model of the background image. The image segmentation step through global thresholding as has been used in the present study can be seen as a region-based segmentation technique that look for regions similar to the background as per Eq. (13). We studied the effect of α which determines the extent of similarity in the sense of a "confidence level" on the background model. Although we have considered a default value of 2.5 for α, any value in the range of 2.0–3.0 was found to work equally well as can be clearly seen from Fig. 12. It may be pointed out that for samples drawn from a normal distribution, a α value in the [2.0 3.0] would represent a confidence limit of about 95% on the background image. Therefore, it is not surprising that the performance of the strategy is not sensitive to α values. We studied the effects of pixel area threshold (ψ_a), and antipod angle threshold (θ_a) as well. Even for a wide range of values, each was found to have only a marginal effect on the accuracy of the results.

5. Conclusions

Traditionally, manufacture of pharmaceuticals and fine chemicals have relied extensively on empirical experience. The lack of understanding of the process and the underlying phenomena arise from complex chemistries, non-availability of detailed models, and the lack of in situ sensors to directly measure product quality. The last issue comes to the fore in particulate processes, for example crystallization, filtration, drying, granulation, etc. While technologies for off-line particle size and shape measurements such as microscopy have been available and are widely used, it is but recently that inline measurements are becoming possible. With the advances in real-time imaging hardware, such as video cameras and fiber optics, and the concomitant developments in image analysis technology, there is an opportunity to control these processes based on direct observation of the product.

A major challenge in online automated image analysis is that in situ images from process equipment are very noisy, therefore segmentation, i.e., separating the particles from the background, is non-trivial. Traditionally, image analysis based approaches have relied on edge detection techniques for particle segmentation, however this requires the specification of suitable thresholds. Specification of robust thresholds is difficult given the high noise and other imperfections in the images. In this paper, we have demonstrated a new method to segment images by combining classical image analysis technique with multivariate statistics. The proposed method takes an alternative approach to segmentation by characterizing the image background instead of the particle. A pseudo-image is first created by extracting suitable features from each in situ image, performing PCA, and formulating the Hotelling T^2 statistic as an image. This pseudo-image has fewer imperfections compared to the in situ image given the noise elimination obtained by ignoring the smaller PCs. It can therefore be segmented robustly using a global threshold. The proposed image analysis strategy uses the background image (without any particle) for estimating this threshold value. The obtained particle outline is further refined through a discrete Fourier transform and signature curve analysis and particle size and shape information extracted.

The accuracy, robustness and efficiency of the strategy have been established by comparing its performance with those obtained by manual image segmentation. The method yields reasonably good estimates of the particles length with about 5% median error. It can therefore be used to reliably investigate crystallization kinetics, especially for high-aspect ratio systems. The availability of real-time measurements of particle length, width and their distribution is also useful for validating crystallization models based on multi-dimensional population balance equations. On an average, each image takes about 6 s to be processed. Therefore, the algorithm is fast enough to provide online measurements of particle size and their distribution for the purpose of online optimization and control of typical crystallization processes.

Notation

a	Fourier descriptors of the boundary
A_X, A_Y	horizontal and vertical kernels for edge detection
B	neighborhood size for feature extraction
d	Euclidean distance between two pixels
E	cumulative error in particle size estimate
$f(x, y)$	image pixel intensity
$g(x, y)$	binary image used for segmentation
K	length of object boundary
N_{FC}	number of Fourier coefficients retained during boundary refinement

N_p	number of PCs retained in the T^2 model
$\bar{\mathcal{O}}$	particle outline
$\mathcal{O}$	refined particle outline
$\hat{\mathcal{O}}$	particle centroid
p	loading vector
r_s	radius (distance) of shifting
$r(\phi)$	signature curve
T	Hotelling's T^2 statistics
X	extended two-dimensional image upon unfolding of $\underline{\mathbf{X}}$
$\underline{\mathbf{X}}$	multi-way image
X^p	pseudo-image used for segmentation

Greek letters

α	threshold parameter indicating confidence level in background model
δ	tolerance factor in accuracy of size estimation
ε	error in particle size estimation
θ_a	antipodal angle threshold
v_k	k^{th} pixel in refined particle outline $\mathcal{O}$
$\bar{v}_k$	k^{th} pixel in particle outline $\bar{\mathcal{O}}$
σ	standard deviation
ψ_a	pixel area threshold
ψ_s	global threshold value for segmentation

Acknowledgment

References

Barrett, P., Glennon, B., 2002. Characterizing the metastable zone width and solubility curve using lasentec FBRM and PVM. Chemical Engineering Research and Design 80, 799–805.

Bartolacci, G., Pelletier Jr., P., Tessier Jr., J., Duchesne, C., Bosse, P., Fournier, J., 2006. Application of numerical image analysis to process diagnosis and physical parameter measurement in mineral processes Part I: Flotation control based on froth textural characteristics. Minerals Engineering 19, 734–747.

Bharti, M.H., MacGregor, J.F., 1998. Multivariate image analysis for real-time process monitoring and control. Industrial Engineering Chemistry and Research 37, 4715–4724.

Bharti, M.H., MacGregor, J.F., Tropper, W., 2003. Softwood lumber grading through online multivariate image analysis techniques. Industrial Engineering Chemistry and Research 42, 5345–5353.

Bharati, M.H., Liu, J.J., MacGregor, J.F., 2004. Image texture analysis: methods and comparisons. Chemometrics and Intelligent Laboratory Systems 72, 57–71.

Braatz, R.D., 2002. Advanced control of crystallization processes. Annual Reviews in Control 26, 87–99.

Calderon De Anda, J., Wang, X.Z., Roberts, K., 2005a. Multi-scale segmentation image analysis for the in-process monitoring of particle shape with batch crystallizers. Chemical Engineering Science 60, 1053–1065.

Calderon De Anda, J., Wang, X.Z., Lai, X., Roberts, K., 2005b. Classifying organic crystals via in-process image analysis and the use of monitoring charts to follow polymorphic and morphological changes. Journal of Process Control 15, 785–797.

Dahl, C.K., Kim, H., Esbensen, K.H., 2007. Image analytical determination of particle size distribution characteristics of natural and industrial bulk aggregates. Chemometrics and Intelligent Laboratory Systems 89, 9–25.

Esbensen, K., Geladi, P., 1989. Strategy of multivariate image analysis (MIA). Chemometrics and Intelligent Laboratory Systems 7 (1–2), 67–86.

Geladi, P., Isaksson, H., Lindqvist, L., Wold, S., Esbensen, K., 1989. Principal component analysis of multivariate images. Chemometrics and Intelligent Laboratory Systems 5 (3), 209–220.

Gonzalez, R.C., Woods, R.E., Eddins, S.L., 2004. Digital Image Processing using Matlab. Prentice-Hall, Upper Saddle River, NJ.

Kempkes, M., Eggers, J., Mazzotti, M., 2007. Measurement of particle size and shape by FBRM and in situ microscopy. Chemical Engineering Science, doi:10.1016/j.ces.2007.10.030.

Larsen, P.A., Rawlings, J.B., Ferrier, N.J., 2006. An algorithm for analyzing noisy, in situ images of high-aspect-ratio crystals to monitor particle size distribution. Chemical Engineering Science 61, 5236–5248.

Larsen, P.A., Rawlings, J.B., Ferrier, N.J., 2007. Model-based object recognition to measure crystal size and shape distributions from in situ video images. Chemical Engineering Science 62, 1430–1441.

Li, M., Wilkinson, D., 2005. Determination of non-spherical particle size distribution from chord length measurements. Part 1: Theoretical analysis. Chemical Engineering Science 60 (12), 3251–3265.

Li, R.F., Thomson, G.B., White, G., Wang, X.Z., De Anda, J.C., Roberts, K.J., 2006. Integration of crystal morphology modeling and online shape measurement. A.I.Ch.E. Journal 52, 2297–2305.

Liu, J.J., MacGregor, J.F., Duchesne, C., Bartolacci, G., 2005. Flotation froth monitoring using multiresolutional multivariate image analysis. Mineral Engineering 18, 65–76.

Ma, C.Y., Wang, X.Z., Roberts, K.J., 2007. Multi-dimensional population balance modeling of the growth of rod-like L-glutamic acid crystals using growth rates estimated from in-process imaging. Advanced Powder Technology 18, 707–723.

Mougin, P., Thomas, A., Wilkinson, D., White, G., Roberts, K.J., Herrmann, N., Jack, R., Tweedie, R., 2003. Online monitoring of a crystallization process. A.I.Ch.E. Journal 49, 373–378.

Patience, D.B., Dell'Orco, P.C., Rawlings, J.B., 2004. Optimal operation of a seeded pharmaceutical crystallization with growth-dependent dispersion. Organic Process Research and Development 8 (4), 609–615.

Puel, F., Marchal, P., Klein, J., 1997. Habit transient analysis in industrial crystallization using two dimensional crystal sizing technique. Chemical Engineering Research and Design 75 (A2), 193–205.

Qu, H.Y., Louhi-Kultanen, M., Kallas, J., 2006. In-line image analysis on the effects of additives in batch cooling crystallization. Journal of Crystal Growth 289, 286–294.

Ruf, A., Worlitschek, J., Mazzotti, M., 2000. Modeling and experimental analysis of PSD measurements through FBRM. Particle and Particle Systems Characterization 17, 167–179.

Sakamoto, K., Rousseau, R.W., 2000. Sizing elongated crystals using a width distribution function: application to aspartame. Industrial and Engineering Chemistry Research 39, 3949–3952.

Wang, X.Z., Calderon De Anda, J., Roberts, K.J., 2007. Real-time measurement of the growth rates of individual crystal facets using imaging and image analysis: a feasibility study on needle-shaped crystals of Lglutamic acid. Chemical Engineering Research and Design 85 (A7), 921–927.

Wang, X.Z., Roberts, K.J., Ma, C., 2008. Crystal growth measurement using 2D and 3D imaging and the perspectives for shape control. Chemical Engineering Science 63, 1173–1184.

Worlitschek, J., Hocker, T., Mazzotti, M., 2005. Restoration of PSD from chord length distribution data using the method of projections onto convex sets. Particle and Particle Systems Characterization 22 (2), 81–98.

Yu, H., MacGregor, J.F., Haarsma, G., Wilfred Bourg, W., 2003. Digital imaging for online monitoring and control of industrial snack food processes. Industrial Engineering Chemistry and Research 42, 3036–3044.

Yu, Z.Q., Chew, J.W., Chow, P.S., Tan, R.B.H., 2007. Recent advances in crystallization control—an industrial perspective. Chemical Engineering Research and Design 85 (A7), 893–905.

Zhou, Y., Srinivasan, R., Lakshminarayanan, S., 2008. Critical evaluation of imaging based techniques for real-time crystal size measurements. Computers and Chemical Engineering (Under review).